Paper II

Christina A. Pedersen, Erich Roeckner, Mikael Lüthje and Jan-Gunnar Winther, "A New Sea-Ice Albedo Parameterization for ECHAM5 General Circulation Model", in preparation for *Journal of Geophysical Research*.

A New Sea-Ice Albedo Parameterization for ECHAM5 General Circulation Model

C. A. Pedersen [a,*] E. Roeckner [b] M. Lüthje [c] J.-G. Winther [d]

[a] *Norwegian Polar Institute and University of Tromsø, Tromsø, Norway*
[b] *Max Planck Institute for Meteorology, Hamburg, Germany*
[c] *Sintef, Stavanger, Norway*
[d] *Norwegian Polar Institute, Tromsø, Norway*

Abstract

Today we experience an accelerated melting of sea ice in the Arctic which global circulation models are inadequate to predict. We believe one of the reasons is the shortcomings in the sea-ice albedo schemes for these models. This paper investigate a physically based sea-ice albedo scheme for ECHAM5 GCM, which separates between snow covered sea ice, bare sea ice, melt ponds and open water (albedos and fractions separately). The new albedo scheme includes important components like albedo decay due to snow aging, bare sea-ice albedo dependent on the ice thickness and a melt pond albedo dependent on the melt pond depth. The explicit treatment of melt pond albedos has to our knowledge never been seen in general circulation models before, and represents a substantial improvement when simulating the annual cycle of sea-ice albedo. The new albedo scheme overall reduce the sea-ice albedo both in winter due to snow ageing and in summer due to melt ponds. The reduced sea-ice albedo leads to overall reduced sea-ice thickness, concentration and volume, with large temporal and spatial variations. In March, some areas experience increased albedo, resulting in thicker sea ice and higher ice concentration, but in August the pattern is more spatially homogeneous with reduced albedo, thickness and concentrations for all areas where the new scheme has a significant effect.

Key words: sea ice albedo, general circulation model, melt ponds

* Corresponding author.
Email address: christina.pedersen@npolar.no (C. A. Pedersen).

In preparation for Journal of Geophysical Research

1 Introduction

The recent increase in human made greenhouse gases have resulted in a substantial change in the global climate with average temperatures in the Arctic increasing twice as much as the global average the last 100 years (ICCP AR4) [Solomon et al., 2007]. Sea-ice used to cover about 15×10^6 km^2 in the northern hemisphere during the maximum period in March-April and 7×10^6 km^2 in the minimum period August-September [Comiso, 2006]. With the increased warming we see substantial decrease both in sea-ice extent and thickness [Gerland et al., 2007]. The Arctic sea ice extent in September declined with an average rate of -7.8% per decade the last 50 years [Stroeve et al., 2007], and with an accelerated trend of -8.6% per decade the last 17 years [Comiso, 2006].

Snow and sea-ice covered surfaces have a high albedo, and are important for the climate whenever large areas are exposed to significant solar energy. Sea ice is particularly sensitive to moderate temperature changes as a warmer climate will expose surrounding surfaces of substantially lower albedo, *e.g.* open water at the expenses of less sea ice [Gerland et al., 2004], thus resulting in most of the incoming sunlight being absorbed, which again leads to further warming. This amplifies the warming and creates a positive feedback [Curry et al., 1995]. Before 2050 the ice albedo feedback is projected to accelerate the Arctic sea ice loss substantially [Gerland et al., 2007].

The sea-ice albedo feedback is very important for the energy balance in general circulation models (GCMs). All GCMs used in the Intergovernmental Panel on Climate Change Fourth Assessment Report (IPCC AR4) show declining Arctic sea ice the last 50 years. However, none or very few, of the models shows trends comparable to the recent observations [Stroeve et al., 2007]. Traditionally, GCMs have treated high-latitude cryospheric processes quite crudely. A diversity of snow and sea-ice albedo parameterizations schemes are currently used in GCMs, see *e.g.* Pedersen and Winther [2005], Curry et al. [2001], Barry [1996] for an overview. Most schemes are very simplistic, depending only on surface type and temperature. A few schemes include snow depth and ice thickness, and even fewer include spectral and solar angle dependencies. However, most GCMs use the sea-ice albedo as a tuning parameter [Curry et al., 2001]. Previous studies have shown that todays GCMs are unable to capture the annual cycle of sea-ice albedo, particularly in summer where the GCMs overestimate the albedo [Køltzow, 2007, Wang et al., 2006, Curry et al., 2001].

A correct representation of sea-ice albedo in GCMs is necessary to incorporate the physical processes involved in the formation and melting of the snow and sea ice, and it has been shown that more advanced schemes allows for larger albedo feedbacks [Curry et al., 2001]. During the northern hemispheric sum-

mer the solar radiation melts the snow and the upper surface of the sea ice and accumulate melt water which later transforms into melt ponds on the ice. These melt ponds substantially reduce the surface albedo and absorb two to three times more solar radiation compared to thick bare sea ice [Fetterer and Untersteiner, 1998b]. We have in this paper suggested a new, more physically based sea-ice albedo parameterization scheme for the ECHAM5 GCM [Roeckner et al., 2006, 2003]. The scheme separates between four surface types (snow covered ice, bare ice, melt ponds and open water) and determines the albedo and fraction of these types separately. To the best of out knowledge, it is the first time the albedo of melt ponds are treated explicit in any GCM.

In short, section 2.1 describes the original temperature dependent sea-ice albedo for ECHAM5, while the new schemes components are presented in Section 2.2. In both experiments the atmospheric composition of greenhouse gases and aerosols was prescribed at constant pre-industrial conditions. This approach allows to create robust statistics as the model is in steady state. Results and intercomparisons of the old and new schemes, both assessing time series and spatial distributions, are given in Section 3. Emphasizes are put on the inclusions of melt ponds. A discussion of the results and conclusions are given in Section 4.

2 Model description of the ECHAM5 general circulation model

The coupled model consists of new model versions for both the atmosphere and the ocean. In the atmosphere model (ECHAM5) [Roeckner et al., 2006, 2003] vorticity, divergence, temperature and the logarithm of surface pressure are represented by a truncated series of spherical harmonics (T31 in this study), whereas the advection of water vapor, cloud liquid water and cloud ice is treated by a flux-form semi-Lagrangian scheme. A hybrid sigma/pressure system is used in the vertical direction (19 layers with the top model level at 10 hPa). The model uses state-of-the-art parameterizations for shortwave and longwave radiation, stratiform clouds, cumulus convection, boundary layer, land surface processes and gravity wave drag.

The ocean model (MPI-OM) [Marsland et al., 2003] employs the primitive equations for a hydrostatic Boussinesq fluid with a free surface. The vertical discretization is on 40 z-levels, and the bottom topography is resolved by means of partial grid cells. The ocean has a nominal resolution of 3° and the poles of the curvilinear grid are shifted to land areas over Greenland and Antarctica. The parameterization of physical processes include along-isopycnal diffusion, horizontal tracer mixing by advection with unresolved eddies, vertical eddy mixing, near-surface wind stirring, convective overturning, and slope convection. The dynamic and thermodynamic sea-ice model is similar to the

earlier HOPE model [Wolff et al., 1997]. The dynamics of sea ice are formulated using viscous-plastic rheology following Hibler [1979]. The thermodynamics relate changes in sea-ice thickness to a balance of radiant, turbulent, and oceanic heat fluxes. The effect of snow accumulation on sea ice is included, along with snow-ice formation when the snow/ice interface sinks below the sea level due to snow loading. The effect of ice formation and melting is accounted for within the model assuming a sea-ice salinity of 5 psu.

In the coupled model [Jungclaus et al., 2006], the ocean passes to the atmosphere the sea surface temperature, sea-ice concentration, sea-ice thickness, snow depth on ice and the ocean surface velocities. The atmosphere runs with these boundary values for one coupling time step (one day) and accumulates the forcing fluxes. These fluxes are then transferred to the ocean. In addition to wind stress, heat and fresh water fluxes, the 10 m wind speed is passed to the ocean for the calculation of the turbulent wind mixing. All fluxes are calculated separately for ice-covered and open water partitions of the grid cells. River runoff and glacier calving are treated interactively in the atmosphere model and the respective fresh water fluxes are passed to the ocean together with the atmospheric precipitation minus evaporation field. A special feature of the coupled model is that the surface wind stress over the ocean is calculated relative to the ocean current. This considerably reduces the cold bias in the equatorial Pacific. The model does not employ flux adjustments.

2.1 The original sea-ice albedo scheme

The sea-ice albedo in ECHAM5 is a function of the ice surface temperature T_i, linearly interpolated between a low albedo at the melting point ($T_i = T_0$) and a larger albedo for cold temperatures ($T_i \leq T_d$) where $T_d = T_0 - 1$ and

$$\alpha_i = \alpha_{i,\min} + (\alpha_{i,\max} - \alpha_{i,\min}) f(T_i) \tag{1}$$

$$f(T_i) = \min\left(\max\left(\frac{T_0 - T_i}{T_0 - T_d}, 0\right), 1\right), \tag{2}$$

where $\alpha_{i,\min}$ and $\alpha_{i,\max}$ are defined separately for bare ice and snow covered ice from Table 1.

Surface type	$\alpha_{i,\min}$	$\alpha_{i,\max}$
Snow covered sea ice	0.60	0.80
Bare sea ice	0.50	0.75

Table 1
Parameters for the original sea-ice albedo scheme for ECHAM5

2.2 The new sea-ice albedo scheme

We take advantage of the knowledge from the model community [Lüthje et al., 2006, Taylor and Feltham, 2004] and combine it with information extracted from field data [Pedersen et al., 2007b, Brandt et al., 2005, Gerland et al., 2004, Perovich et al., 2002b, Gerland et al., 1999, Morassutti and Le Drew, 1996]. We follow the structure of the complex parameterization of a small scale thermodynamic model [Schramm et al., 1997] to construct a new sea-ice albedo scheme for the surface types; snow covered sea ice (α_s), bare sea ice (α_i), melt ponds (α_{mp}) and open water (α_w), where the total sea-ice albedo is weighted according to the respective fractions

$$\alpha = \alpha_s f_s + \alpha_i f_i + \alpha_{mp} f_{mp} + \alpha_w f_w. \tag{3}$$

ECHAM5 originally only separates between open water (f_w) and (snow covered) sea ice, so the snow covered sea-ice fraction is modified to include snow covered sea ice (f_s), bare ice (f_i) and melt ponds (f_{mp}) by determining the relative fractions accounting for the ice concentration.

In the latest version of ECHAM5, the numbers of spectral bands has been increased to six (three bands in the UV-visible (VIS) and three bands in the near infrared (NIR)), however, here the same parameterizations are used for the three VIS bands and the three NIR bands. Separate schemes are developed for the diffuse and direct components of the solar radiation [Wiscombe and Warren, 1980, Warren, 1982], and weighted according to the cloud cover fraction

$$\alpha_x = f_{dir} \cdot \alpha_{x,dir} + f_{dif} \cdot \alpha_{x,dif}, \tag{4}$$

where the fraction of direct (f_{dir}) and diffuse (f_{dif}) radiation is computed from ECHAM5, and $\alpha_{x,dir}, \alpha_{x,dif}$ are the direct and diffuse part of the surface type in question, respectively. The individual albedo components, described in the next sections, are also summarized in Table 4.

2.2.1 Snow covered sea ice

Much effort has been on modeling the albedo of snow-covered land. Two main groups of snow albedo schemes are predominant for GCMs: temperature dependent schemes (which includes ECHAM5) and prognostic schemes. In a previous study the temperature dependent schemes was found not to capture the winter snow metamorphosis and spring melting very well as the albedo was fixed to its threshold values [Pedersen and Winther, 2005]. Also a common deficiency for temperature dependent schemes is the peak of error during the onset of melt [Køltzow, 2007]. The prognostic schemes have an iterative albedo dependence, with separate decay factors for melting and non-melting

snow and reset the albedo to its maximum after new snowfall above a prescribed precipitation threshold, and is found to capture the seasonal cycle better than the temperature dependent schemes [Pedersen and Winther, 2005]. Another study identified the simplest and strongest relationship for albedo decay between mean albedo and the day number following a snowfall [Baker et al., 1990].

Both types of schemes were originally created for use for snow on land, but can equally well be used for snow covered sea ice, by compensation for an underlying surface of bare sea ice. We suggest to replace the original, empirical temperature dependent scheme in ECHAM5 with a more physically based prognostic scheme. The choice fall on the prognostic snow albedo scheme BATS [Dickinson et al., 1986], which includes all processes relevant to capture the changes in snow albedo. It was proven to accurately represent the temporal snow albedo decay when implemented in ECHAM4, BATS was in fact the preferred snow albedo scheme for ECHAM4 [Roesch, 2000]. It separates between VIS and NIR bands as well as diffuse and direct radiation. The BATS snow albedo model is publicly available on the web, has been distributed to over 100 users, and is currently being used in numerous projects [SMIP, 2006]. The BATS snow scheme has been validated against observations in Roesch [2000], Yang et al. [1997] with good correspondence. No additional work has been performed on validating nor improving the snow cover fraction, and it is parameterized according to ECHAM5s original [Roesch et al., 2001].

2.2.2 Bare sea ice

Less effort has been put into the modeling of bare sea-ice albedo, which is natural since the sea ice is snow covered during most of the cold winter period. However, as there is little or no Sun for the northernmost Arctic during the cold winter, despite the period with bare sea ice being shorter in duration it contribute major to the energy balance because of much irradiance.

We are taking advantage of the extensive sets of sea-ice albedos collected by Brandt et al. [2005] in the Antarctic sea-ice zone over several years. The spectral albedos for different sea-ice types were measured and converted into VIS ($\lambda < 700$ nm) and NIR ($\lambda > 700$ nm) sea-ice albedos (Figure 1). As the clouds absorbs only weakly at visible wavelengths, Brandt et al. [2005] used that the visible albedo is the same under cloudy and clear skies (for an average solar zenith angle of about 60°), while for NIR, the observations were split into a diffuse and direct component. Based on their observations we propose a simple LMS fit parameterization of the form

$$\alpha_i = a \cdot \log(h_i) + b, \tag{5}$$

where a and b are the model parameters and h_i is the ice thickness in cm

(Table 2). For ice thicknesses equal to or above 1.6 m for VIS and 1.0 m for NIR, the upper threshold values from Table 2 are used.

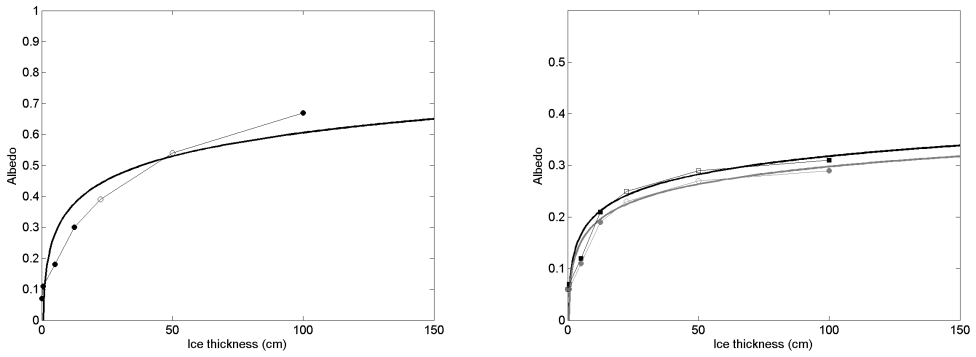

(a) VIS (b) NIR

Fig. 1. Sea-ice albedo as a function of ice thickness for (a) visible (VIS, $\lambda < 700$ nm) and (b) near infra-red (NIR, $\lambda > 700$ nm) spectral bands after [Brandt et al., 2005]. The filled symbols are actually measurements, while the open are interpolated values. The depths are mean of the range of each sea-ice type. The thick solid line is the LMS fit of the form $\alpha_i = a \cdot \log(h_i) + b$ (Table 2). A distinction is made between direct (upper curve in black) and diffuse (lower curve in gray) irradiance for NIR in (b).

	a	b	Upper threshold
VIS	0.13	0.10	0.76
NIR Direct	0.047	0.074	0.29
NIR Diffuse	0.049	0.085	0.31

Table 2
Constants for bare sea-ice albedo of the form $\alpha_i = a \cdot \log(h_i) + b$ proposed from data from Brandt et al. [2005] for visible (VIS, $\lambda < 700$ nm) and near infra-red (NIR, $\lambda > 700$ nm) (direct and diffuse). The upper threshold values are used for ice thickness equal to or above 1.6 m for VIS and 1.0 m for NIR.

2.2.3 Melt ponds

The inclusion of melt ponds in the albedo parameterization scheme is very important from a physical perspective, due to their extensive presence during summer [Perovich et al., 2002b, Tschudi et al., 2001, Fetterer and Untersteiner, 1998b, Perovich and Tucker, 1997]. However, to our knowledge currently no GCM include an explicit formulation of melt ponds. Both Schramm et al. [1997], Morassutti and Le Drew [1996] have provided useful albedo schemes of melt pond albedo as a function of pond depth. However, these can not be used

directly as melt pond depth, and also the more important melt pond fraction (cf. Eq. (1)) is not available in ECHAM5 (or other GCMs).

Melt ponds have been investigated at several locations in the Arctic over the years at ground [Tucker et al., 1999, Fetterer and Untersteiner, 1998b, Perovich and Tucker, 1997], from air [Perovich et al., 2002b, Tschudi et al., 2001, Derksen et al., 1997] and from space [Markus et al., 2003, 2002, Hanesiak et al., 2001b, Yackel and Barber, 2000]. Also, the seasonal evolution of melt ponds have been modeled [Lüthje et al., 2006, Taylor and Feltham, 2004]. The above mentioned studies indicate a melt pond fraction ranging from 5-80% depending on surface roughness, snow cover, time of year, ice type and location. The spatial distribution of melt ponds depends on topography of the snow and sea ice, and first year ice (FYI) tend to be smoother than multi year ice (MYI), and melt ponds on FYI are normally less deep [Morassutti and Le Drew, 1996], but cover a larger area [Hanesiak et al., 2001a]. The formation of melt ponds on FYI is strongly correlated with the winter distribution of snow, and areas of little snow during winter are preferred places for melt ponds to form [Hanesiak et al., 2001a, Derksen et al., 1997]. On the rougher MYI the melt ponds form in depressions, and tend to be smaller, deeper and more numerous.

We propose a plain model for melt pond evolution based on the daily surface ice melt rate calculated from ECHAM5. The temporal evolution of a melt pond is calculated from the following mass balance equation

$$\frac{\partial p_d}{\partial t} = -\frac{\rho_i}{\rho_w}\left(\frac{\partial h_i}{\partial t} + \frac{\partial p_{di}}{\partial t}\right) - \left(\frac{\partial p_d}{\partial t}\right)_s \tag{6}$$

where p_d is the pond depth in m and ρ_w, ρ_i are the densities of water and ice, respectively (Figure 2). The first term on the r.h.s. represents the melt pond growth through the surface melting of sea ice. The second term refers to the growth or melting of pond ice, where the last term is a constant seepage rate. Pond ice forms if the temperature of the pond T_w falls below the freezing point T_0 where T_w is calculated from the heat budget equation

$$C_w \frac{\partial T_w}{\partial t} = H_{sfc}. \tag{7}$$

C_w is the heat capacity of the pond and H_{sfc} is the sum of all radiative and turbulent heat fluxes at the surface of the ice-free pond. For $T_w < T_0$, a slab of ice is formed according to

$$p_{di} = \left(\frac{C_w}{L_f \rho_i}\right)(T_0 - T_w), \tag{8}$$

where L_f is the latent heat of fusion. T_w is then reset to T_0 and is kept fixed, independent of the sign of H_{sfc}, because the pond water is forming on top of

the sea ice. The surface temperature of the ice, T_i, is calculated from the heat budget of a thin slab of ice (1 cm) at the surface

$$C_i \frac{\partial T_i}{\partial t} = H_{sfc} + H_{con}, \tag{9}$$

where C_i is the heat capacity of a thin upper slab of pond ice (1 cm) and H_c is the conductive heat flux through the ice given by

$$H_c = \frac{\kappa_i}{p_{di}}(T_0 - T_i) \geq 0, \tag{10}$$

where κ_i is the thermal conductivity of ice.

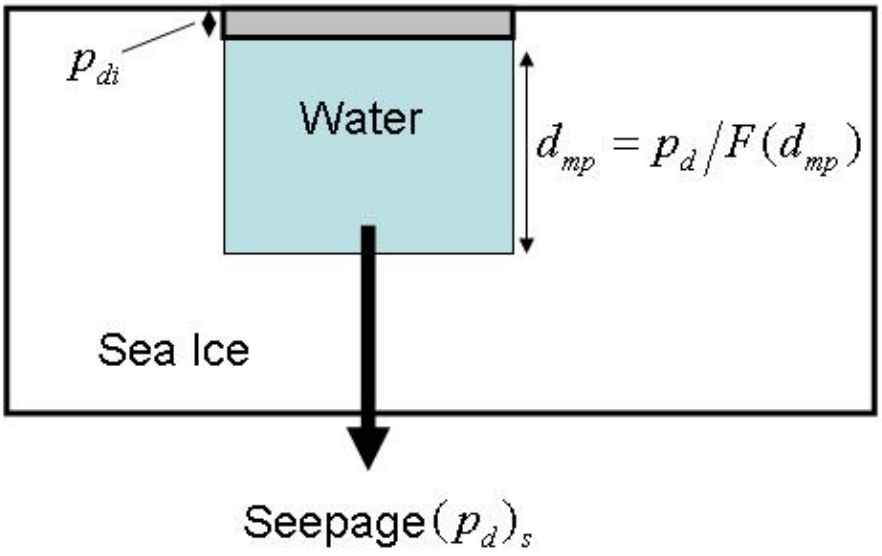

Fig. 2. A schematic drawing of a melt pond describing the variables in Equations 6-10.

Melt pond formation will not start before the snow on top of the sea ice has melted away. If a slab of pond ice $p_{di} \geq 1$ cm is forming, the melt pond fraction is set to zero. The final closing of the melt pond in fall is generally caused by vanishing melting and constant seepage, resulting in $p_d \leq 0$, or by freezing if the pond is totally frozen or if a thick ice layer has been formed ($p_{di} = 10$ cm). In all these cases the pond is closed, *i.e.*, p_d is set to zero.

The melt pond fractions are calculated from the melt pond depths using a parameterization based on simulations from a small-scale melt pond model [Lüthje et al., 2006]. This model, developed to investigate the area evolution of melt pond on sea ice, uses the topography of the sea-ice area as input. The area is divided into cells and the melt rate for the ice surface and seepage is set as constant parameters. The ice surface is treated as a porous medium and

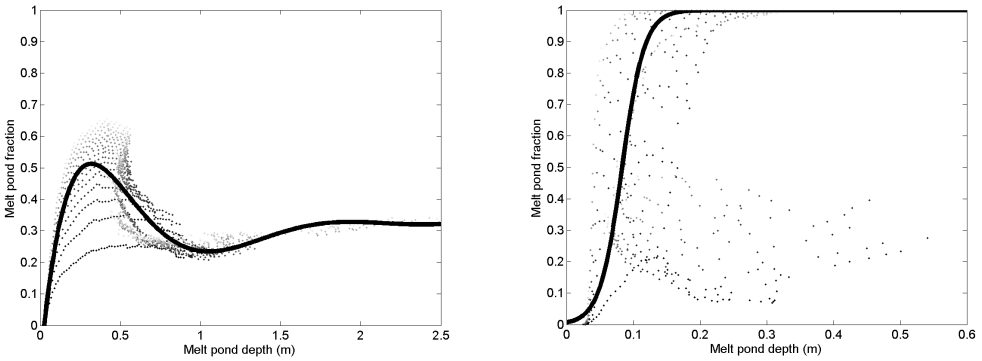

(a) (b)

Fig. 3. Melt pond depth versus melt pond fraction for (a) multi year ice (MYI) and (b) first year ice (FYI). The thick lines represents the best fit to the data. For MYI the best fit is represented by a 8-degree polynomial (Eq. (11)), and for FYI by a hyperbolic tangent (Eq. (13)). The scatter plot is for several melt rates, with lighter color corresponding to higher melt rates (ranging from 1-3 cm/day.

melt water left on the surface percolates to lower lying areas to form melt ponds. The melt rate is enhanced where melt ponds forms. In addition to sea ice topography, seepage rate of melt water and melt rate of the sea-ice surface, the model uses the ice surface permeability and the enhancement of melt rate beneath the melt pond as input parameters. In this case, the model was run with the same settings of permeability (9×10^{-9} m^2) and seepage rate (0.8 cm/day) as described in Lüthje et al. [2006]. However, the melt rate for the ice surface was varied in steps of 0.1 cm/day from 1.0 cm/day to 3.0 cm/day while the enhanced melt rate under the melt ponds was kept to twice the ice surface melt rate. The model was run for 71 days resulting in the scatter plots of the melt pond fraction against melt pond depth for FYI and MYI, separately, in Figure 3. To link the melt pond depth to the melt pond fraction for MYI, the data was best fitted to a 8-degree polynomial of the form:

$$\begin{aligned} F(d_{mp}) = &- 0.00724636 d_{mp}^8 + 0.14438 d_{mp}^7 - 1.19140 d_{mp}^6 + 5.25995 d_{mp}^5 \\ &- 13.37101 d_{mp}^4 + 19.53030 d_{mp}^3 - 15.27019 d_{mp}^2 + 5.26674 d_{mp} \\ &- 0.12549, \end{aligned} \tag{11}$$

where d_{mp} is the melt pond depth in m. The relative depth in the melt pond d_{mp} is related to the grid cell depth in ECHAM5 (p_d) from

$$d_{mp} = \frac{p_d}{F(d_{mp})}. \tag{12}$$

Figure 3b shows the rather complex connection between depth and fraction for FYI depending on the time of the season (pond formation increasing or decreasing). A hyperbolic tangent function was fitted to the FYI data,

$$F(d_{mp}) = 0.5 \tanh(30 d_{mp} - 2.5) + 0.5 \tag{13}$$

corresponding well with the results for relative shallow ponds, but unable to capture the scatters for deeper ponds. However, melt ponds on FYI tend to be quite shallow and when deeper melt ponds are formed, they often coincide with the break up of the ice. Therefore the important phase of the formation of melt ponds on FYI is in the beginning of the melting period.

Regression equations were used for calculating the melt pond albedo from melt pond depth, based on 500 observations of melt pond albedo in the Canadian Arctic Archipelago in spring and summer 1994 [Morassutti and Le Drew, 1996]:

$$\alpha_{mp} = a + \exp(-b \cdot d_{mp} - c), \tag{14}$$

where a, b and c are regression coefficients, subtracted for VIS (400-700 nm) and NIR (700-1000 nm) bands under different lighting conditions (Table 3). The exponential albedo decay is large for the first 10-20 cm of pond water, but for deeper melt ponds the albedo is almost constant.

	a	b	c
VIS Direct	0.336	9.457	1.061
VIS Diffuse	0.413	24.014	1.086
NIR Direct	0.017	18.904	0.909
NIR Diffuse	0.061	17.449	1.075

Table 3
Constants for melt pond albedo of the form $\alpha_{mp} = a + \exp(-b \cdot d_{mp} - c)$ from Morassutti and Le Drew [1996] for visible (VIS) and near infrared (NIR) and direct and diffuse radiation.

3 Results

Two model experiments were performed using a low-resolution version of ECHAM5/MPI-OM [Jungclaus et al., 2006]. The atmospheric component, ECHAM5, has a horizontal resolution of T31 in spectral space, corresponding to a grid of 3.75°x3.75°, with 19 layers in the vertical. The oceanic component, MPI-OM, has a horizontal resolution of 3° and 40 layers in the vertical. In the first experiment (CTL), the original temperature-dependent sea-ice albedo scheme (cf. Sec. 2.1) was used. In the second experiment (ALB), the new albedo scheme (cf. Sec. 2.2) was applied. In both experiments the atmospheric composition of greenhouse gases and aerosols was prescribed at constant pre-industrial conditions. The experiments started from the same initial state obtained from a multi-century simulation with the standard configuration of the model and were both run for another 100 years. During this period the climate drift in global mean climate parameters is negligible. For

Albedo of surface type	VIS 250-690 nm	NIR 690-4000 nm
Snow covered sea ice, α_s		
Direct	BATS equations	BATS equations
Diffuse	BATS equations	BATS equations
Bare sea ice, α_i		
	$0.13\ln(h_i) + 0.10^*$	
Direct		$0.047\ln(h_i) + 0.074^*$
Diffuse		$0.049\ln(h_i) + 0.085^*$
Melt pond, α_{mp}		
Direct	$0.336+$ $\exp(-9.457d_{mp} - 1.061)$	$0.017+$ $\exp(-18.904d_{mp} - 0.909)$
Diffuse	$0.413+$ $\exp(-24.014d_{mp} - 1.086)$	$0.061+$ $\exp(-17.449d_{mp} - 1.075)$

Table 4
The new sea-ice albedo parameterization scheme in ECHAM5, separating between snow covered sea ice, bare sea ice, melt ponds and open water (corresponding to ECHAM5's original, and therefore not repeated here), for visible (VIS) and near infrared (NIR) bands and diffuse and direct radiation. h_i is the ice thickness in cm, and d_{mp} is the melt pond depth in m. * For ice thicknesses equal to or above 1.6 m for VIS and 1.0 m for NIR, constant albedos of 0.76 for VIS and 0.29 for NIR direct and 0.31 for NIR diffuse are used.

example, in both experiments, the linear trend in global mean near-surface temperature is smaller than 0.01 K/century. For the analysis, only the last 50 years of the simulations were considered. The climatological means as well as the standard deviations shown in the figures refer to this 50-year time series.

3.1 Seasonal cycles

3.1.1 One year seasonal cycle

First, the seasonal cycle of the new albedo scheme were investigated for a single sea-ice grid cell for one year (Figure 4a). The chosen grid cell was within the multi year sea ice at 76°N and 165°W. The snow cover fraction was one until mid-June, hence the sea-ice albedo is completely determined by the prognostic snow albedo scheme, which is high and fluctuates around the mean of 0.79 from

January to May. The periodic events with reductions and growths are due to the ageing of the snow and new snow fall events, respectively. The basic ageing factor f_{age} in the snow albedo scheme (Sec. 2.2.1) is never completely reset to zero during winter (however, it reach values down to 0.02 after large snow events). From May and onwards the ageing parameter increase and in mid-June it reaches maximum above 0.7, resulting in a steady decay in albedo. The snow cover fraction falls from one to zero in a short time period in mid-June, when the snow water equivalent (SWE) snow depth falls from 4 cm to 0 cm. This fall coincident with the steep decay in snow albedo at the same time. Simultaneously, the bare ice fraction jumps to one, giving an albedo completely determined by the ice albedo (Sec. 2.2.2). A few weeks after the abrupt snow melting, melt water has formed and creates melt ponds on the ice. As the fraction of melt ponds increase and the melt ponds get deeper, the surface albedo decreases. The melt pond fraction peaks in early August. In the end of August the ponds start to dry up, and the melt pond fraction decrease. Light snowfall in the beginning of September increase the albedo again. The first real autumn snowfall provides only 1 cm SWE, however such a thin snow cover is often inhomogeneous, and the snow cover fraction was only 0.1-0.2. For ECHAM5, a snow depth above 3 cm SWE gives a snow cover fraction of one, implying "optically thick" snow [Wiscombe and Warren, 1980]. In mid September a major snow event increase the snow cover fraction to one and provides albedos comparable to pre-melting conditions.

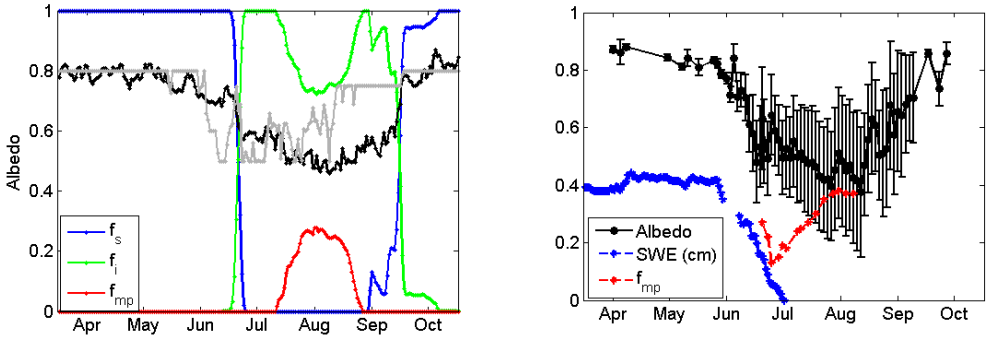

(a) (b)

Fig. 4. Seasonal cycle of (a) sea-ice albedo for the new (ALB, black) and old (CTL, grey) schemes at the SHEBA site in the multi year ice Arctic Ocean. Also shown are the area fractions (see legend, where f_s is snow covered sea-ice fraction, f_i is bare ice fraction and f_{mp} is melt pond fraction). (b) Observed sea-ice albedo (mean and standard deviations in black) along the 200 m "albedo-line" at SHEBA in 1998. Also shown is the snow depth (in SWE) and the melt pond fractions at the SHEBA site.

Some clear differences are identified by comparing ALB and CTL albedo schemes (Figure 4a). CTL is constant at 0.8 when temperatures are below freezing, hence it is basically at this value from mid-September until June,

with only one drop in mid-May due to a short period of warm temperatures, while the ALB albedo vary due to snow ageing and new snow falls, as described above. In spring and early summer when the surface temperature topple above zero, and the snow cover fraction still is at one, the CTL albedo is immediate fixed to its lower snow value, long before the steep decay in ALB albedo due to the snow melting. For snow free conditions, the CTL albedo is completely determined by the sea-ice albedo fluctuating between 0.5 and 0.75. Hence the CTL albedo is higher than the ALB albedo during most of the summer. Particularly, in spring and late summer, the ALB albedo deviates substantially from CTL albedo; in late summer ALB albedo is significantly lower due to the inclusions of melt ponds.

The chosen grid cell within the multiyear ice with an average thickness of 3 m, includes the positions of the SHEBA ice camp in summer in 1998 [Perovich et al., 1999]. Figure 4b shows the measured sea-ice albedo and standard deviations along the 200 m "albedo-line" at SHEBA in 1998 [Perovich et al., 2002a]. The seasonal evolution of the albedo from the SHEBA site is throughly discussed in Perovich et al. [2002a], and consists of five distinct phases: dry snow, melting snow, melt pond formation, melt pond evolution and fall freeze-up (Figure 4b). The SHEBA albedo was a combination of gradually changes due to seasonal evolutions and abrupt changes due to synoptic weather events. A different mixture of sea-ice types along the albedo line would only change the magnitude of the albedo, not the temporal behavior [Perovich et al., 2002a], so it is appropriate to compare the time series of ALB albedo with the observed albedo at SHEBA. However, keep in mind that modeled albedo cycle can not be linked to any particular year.

The ALB albedo corresponds well with the SHEBA observations in terms of trends, with a correlation coefficient of 0.83, and an average root mean square error of 0.08. The absolute numbers are not of immerse importance as a delay of spring melting and/or fall freeze-up can appear in any of the two datasets because of interannual variability and synoptic weather events. The ALB albedo is lower than the observed albedos at SHEBA during winter, early spring and late fall when snow is present. In summer, it is opposite. Both time series show a rather steep decline in the albedo starting in late spring and reaching its minimum when the melt pond fraction reaches its maximum. However, the abrupt change is a combination of melting snow and formation of melt ponds in SHEBA [Perovich et al., 2002a], while it is linked to melting of the snow and decreasing snow cover fraction in ECHAM5. Since the melting of snow coincided with the melt pond formation in SHEBA it is difficult to separate the effect of the two. Recall that melt ponds do not form on the ice before the snow is completely melted (Sec. 2.2.3). Just after the ice becomes snow free, a slight increase can be observed in the albedo due to whitening of the ice (S. Gerland, personal communication). The average melt pond coverage over the entire melt season at SHEBA was 32% for level

MYI and 13% for rough MYI [Eicken et al., 2004]. The ALB scheme does not differ between FYI and MYI, but over the period where melt ponds were present, the average coverage was 19%. The maximum melt ponds coverage (28%) took place 20 days after the first ponds formed. This is higher than observed maximum coverage for rough MYI (21%), but lower than observed on level MYI (46%) [Eicken et al., 2004]. The modeled mean melt pond depth of 35 cm in August fits well to observations [SHEBA melt pond, 2007].

3.1.2 Average seasonal cycles

The area fractions (snow covered sea ice, bare ice and melt ponds) for the 50-years average over northern hemisphere (NH, Figure 5a) show a different characteristic compared to the one year for one grid cell discussed above, where the abrupt changes in the one year timeseries are replaced with more gradual changes. The NH winter is characterized with mostly snow covered sea ice. Due to time and space averaging, the snow fraction is below one during winter, as weather events can bring warm air which melts away the snow near the ice edges. In July and August the ice fraction is at its maximum at 0.72 ± 0.03, while the snow fraction is at its minimum. The standard deviations for snow covered and bare ice are small and relative constant at 0.05 during the seasonal cycle. Melt ponds start to form in May and are present until September. The mean coverage for July and August are 26% and 23%, respectively, both with a standard deviation of 4%.

The area fractions and thereby the dominant sea-ice types have a completely different pattern for the southern hemisphere (SH, Figure 5b), with large variabilities in the snow covered and bare sea-ice fractions in Antarctic summer (January and February). This is due to the large interannual variability with much snow in relatively cold summers and less snow in warm summers on the ice edges. Melt ponds cover a much smaller area in the SH, and is only present in January and February, with a mean melt pond coverage of 4% in the peak of the SH summer. Observations of melt pond coverage in the SH is very limited, but the overall coverage is small [Brandt et al., 2005, Andreas and Ackley, 1982, personal communication with C. Haas] because the ice tend to melt predominantly from the bottom and up due to a higher heat flux from the ocean. In the long Antarctic winter snow completely covers the sea-ice, with snow cover fraction as high as 0.995 in September (different from the relatively lower snow cover fraction in NH in winter).

The annual average sea-ice albedo is 0.66 in the NH and 0.76 in the SH, with standard deviations of 0.04 and 0.01, respectively. The seasonal cycle of sea-ice albedo is shown in Figure 5c. Overall, the ALB scheme reduces the albedo for all seasons for NH, with as much as 10% on average for summer (May to October). The largest reductions (23% and 15%) appear in August

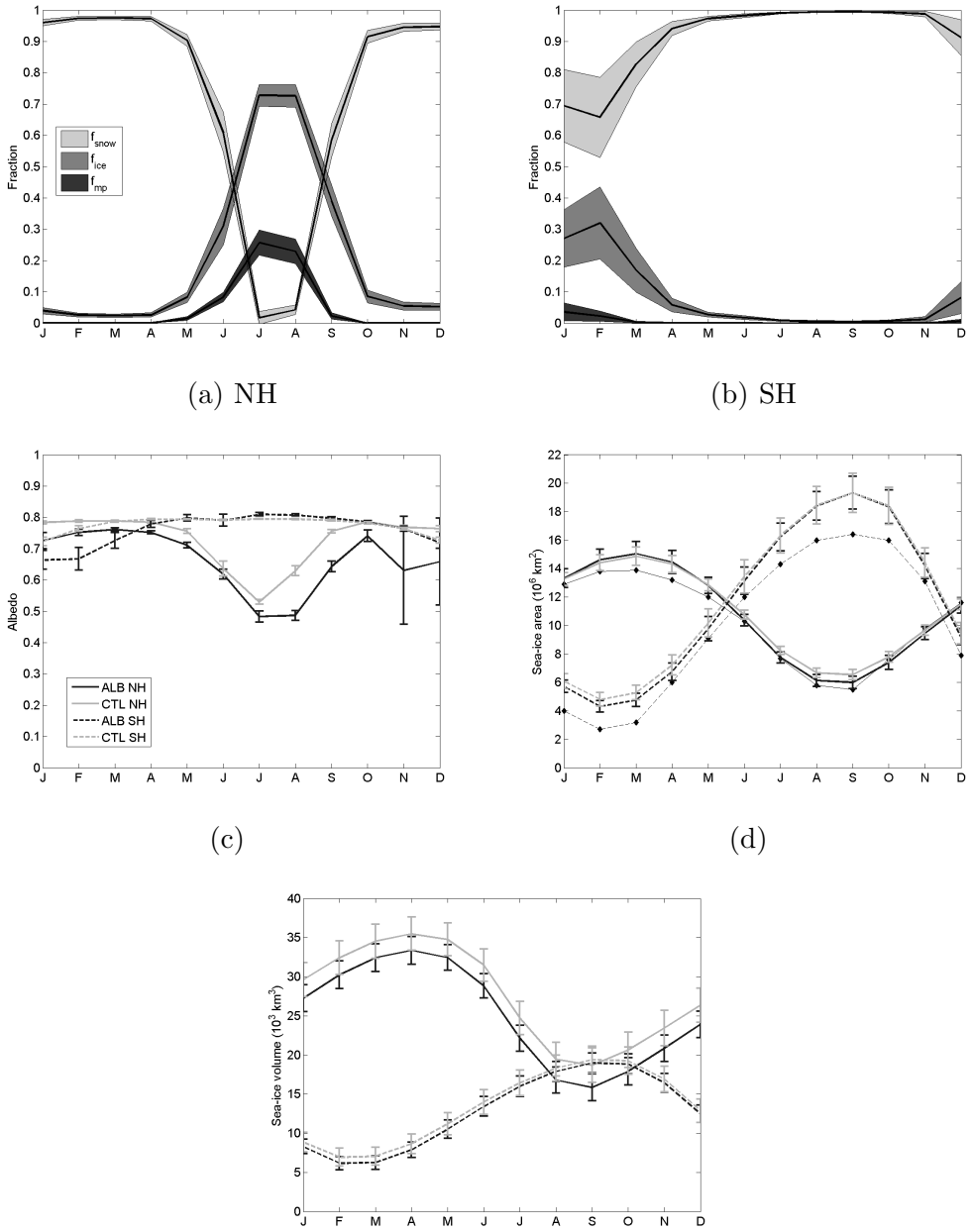

Fig. 5. 50 years average seasonal cycles of area fractions (snow covered ice: f_{snow}, bare ice: f_{ice} and melt ponds: f_{mp}) and standard deviations (as shades) for northern hemisphere (NH) in (a) and southern hemisphere (SH) in (b) for the new (ALB) albedo scheme. 50 years means and standard deviations (as error bars) of sea-ice albedo in (c), sea-ice area in (d) and sea-ice volume in (e) for old (CTL) and new albedo scheme for NH and SH. The diamonds in (d) are average sea-ice area from HadISST [Rayner et al., 2003].

and September, respectively. The ALB scheme has a relative low albedo in NH winter, probably due to snow ageing (as the description of the snow cover fraction is common for CTL and ALB schemes). The snow albedo has the potential to drop relatively low in winter for weather situations with no or little snowfall. The new snowfall parameter resetting the albedo and snow age to its maximum values is of immerse importance, and we plan to investigate this further with sensitivity simulations. The smallest changes due to the ALB scheme is in March and June with only 3% reduction. The sea-ice albedo have large interannual variabilities for November and December. This is yet not fully understood. However, in summer the ice concentration in the Arctic is relatively small (around 0.7, not show here) compared to satellite data (0.9). In fall and early winter the open water areas are re-frozen and the compactness increase. Although the total NH sea-ice areas show little interannual variability in November and December (Figure 5d), there might be regional variability due to atmospheric and/or ocean dynamics. For SH, the seasonal sea-ice albedo cycle is relatively weak, with albedos above 0.7 for all months, except January and February. This results in less pronounced albedo reductions. The winter snow albedo is higher in SH compared to NH, because the snow ageing in BATS is smaller in SH compared to NH (r_3 is 0.01 in SH, and 0.3 in NH [Dickinson et al., 1993]). In SH summer (January and February) the maximum reduction is 13%. As the melt pond fraction is relatively small comperd to NH in summer (and the highest fraction is for snow covered sea ice), the decrease in albedo is probably a combination of the melt ponds on the ice and lower snow albedo due to snow ageing and relatively high temperatures. For May and July-November, the ALB albedo scheme slightly increases the albedo compared to the CTL scheme (on average a 1% rise).

The annual mean areas of sea ice is 10.7×10^6 km^2 in the NH and 11.6×10^6 km^2 in the SH, with standard deviations of 0.56×10^6 km^2 and 0.79×10^6 km^2, respectively. The seasonal cycle of sea-ice area in the ALB scheme (with the CTL scheme following closely) have maximums of $15.1\times$ 10^6 km^2 in March for NH and $19.3\times$ 10^6 km^2 in September for SH. The minimums are at $6.0\times$ 10^6 km^2 in September and $4.3\times$ 10^6 km^2 in February, respectively (Figure 5d). The seasonal cycle in the SH span a larger range, implying that the SH has substantial more FYI compared to the NH. The ALB scheme leads to increased sea-ice area in NH winter (on average 1% or 0.14×10^6 km^2). From May and onwards the trend is opposite with reduced sea-ice area. The largest reductions are found in August and September with 8% reductions or 0.55×10^6 km^2). The effect in SH is reduced sea-ice area for all months, except September, which has an insignificant increase. The differences are largest in February and March with an average sea-ice area reduction of 10% or 0.51×10^6 km^2.

Compared to HADISST sea-ice area [Rayner et al., 2003] over the years 1979-2002 the seasonal cycle is in phase (correlation coefficients as high as 0.99 for both NH and SH), but with offset amplitudes. Overall the sea-ice areas

from model simulations (both ALB and CTL) are higher than the HADISST area (particularly for SH), except for June-July and October-December in NH, where the ALB scheme matches HADISST or are slightly lower, respectively. Overall, the ALB scheme is 3.7% higher than HadISST for NH and as much as 16.1% higher for SH. The difference between present and pre-industrial climate may, however, be responsible for some of this deviation.

The annual mean sea-ice volume is 25.2×10^3 km^3 for the NH and 12.8×10^3 km^3 for the SH, with standard deviations of 1.70×10^3 km^3 and 1.12×10^3 km^3, respectively. The seasonal cycle of ice volume is shown in Figure 5e. The new ALB scheme affect the sea-ice volume substantially more in NH than SH. The annual average volume decrease is 10% for NH compared to 5% for SH, corresponding to 2.6×10^3 km^3 and 0.7×10^3 km^3 reductions, respectively. The reductions in volume is relatively much larger than reductions in sea-ice areas, particularly for NH due to large reductions in ice thickness.

3.2 Spatial distributions

We just showed that the new ALB scheme overall reduced the sea-ice albedo, area and volume, mostly in the NH, and mostly in summer, and we will now investigate the spatial distributions. When describing the areas in NH we will use the area mask of Arctic Basin marginal seas and seasonal ice zones from Overland and Wang [2007].

3.2.1 Melt ponds

Observations show that melt ponds in the NH typically cover around 20%-35% for MYI [Tschudi et al., 2001, Fetterer and Untersteiner, 1998a, Tschudi et al., 1997] and 45%-80% for FYI [Yackel and Barber, 2000, Yackel et al., 2000, Barber and Yackel, 1999]. The average coverage in ALB is within this range with coverage of 26% and 23% in July and August, respectively. Figure 6 shows for the first time a modeled estimate of the spatial variability of the melt pond coverage. The spatial pattern shown that most melt ponds are found close to land, with highest fractions in southern Barents, northern Baffin Labrador and along east Greenland. North of 80°N the fractional coverage is much smaller. The deepest melt ponds are found in the E. Siberia Chukchi and Beaufort whereas the melt ponds are shallower to the north. The ALB scheme predicts melt ponds along the souther east coast of Greenland, which is not in accordance with observations, as the sea ice in those areas are mostly is pancake ice.

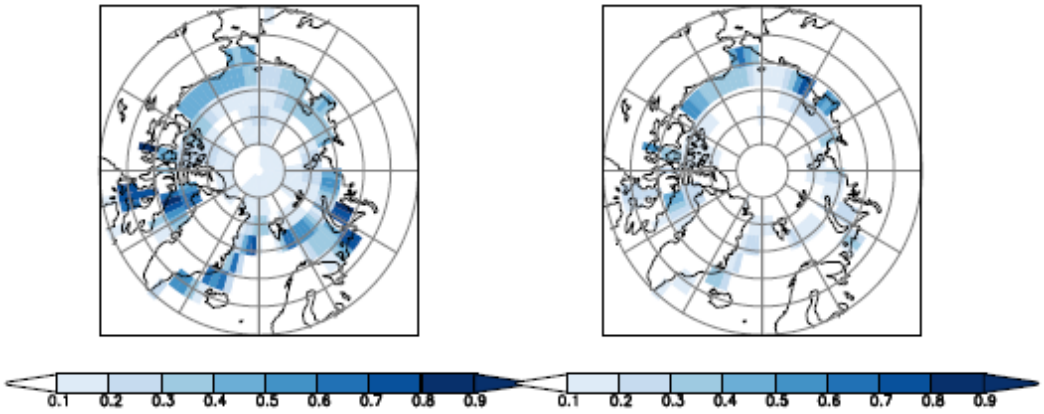

Fig. 6. Spatial variabilities of the melt pond fractions (left) and the melt pond depths averaged over the sea ice area (p_d, m, right) for the northern hemisphere for July.

3.2.2 Sea-ice albedo

The sea-ice albedo is high (average 0.78) and relative homogeneous over the Central Arctic in March (Figure 7). Only in south Baffin Labrador, Bearing and Okhotsk the albedo takes somehow lower values. The effect of the ALB scheme is to reduce the albedo everywhere, except Okhotsk and small areas north of Norway and in Hudson Bay, where the ALB scheme leads to increased albedos. For some areas in Central Arctic and Kara Laptev no changes are evident. For August the ice covered areas are substantially smaller, with reduced albedo everywhere (average reductions of 0.1). The average sea-ice albedo in the Central Arctic is 0.45, and around 0.3 on the ice edge. For some areas, *e.g.* around the south and east coast of Greenland, ALB completely melts the ice, hence the albedo reductions are substantial.

The sea-ice albedo varies between 0.2 for mixed pixels on the ice edge to above 0.7 for SH summer (March, Figure 8). The ALB scheme reduces the albedo for all ice covered areas, except one pixel in the Weddell sea (probably caused by sampling artifacts). In August the sea-ice area is larger, and the albedo is relative high except on the ice edge. For this month the effect from the ALB scheme has a different characteristic, with increased albedo around the Antarctic continent, and decreased albedo to the north and east.

3.2.3 Sea-ice thickness

The average sea-ice thickness in the Central Arctic from the ALB scheme is around 3.3 m in March, and is reduced by 0.2-0.3 m in September (Figure 9). The ice is thickest in the E. Siberia Chukchi and in Central Arctic towards Greenland and east Canada in March (corresponding well with other

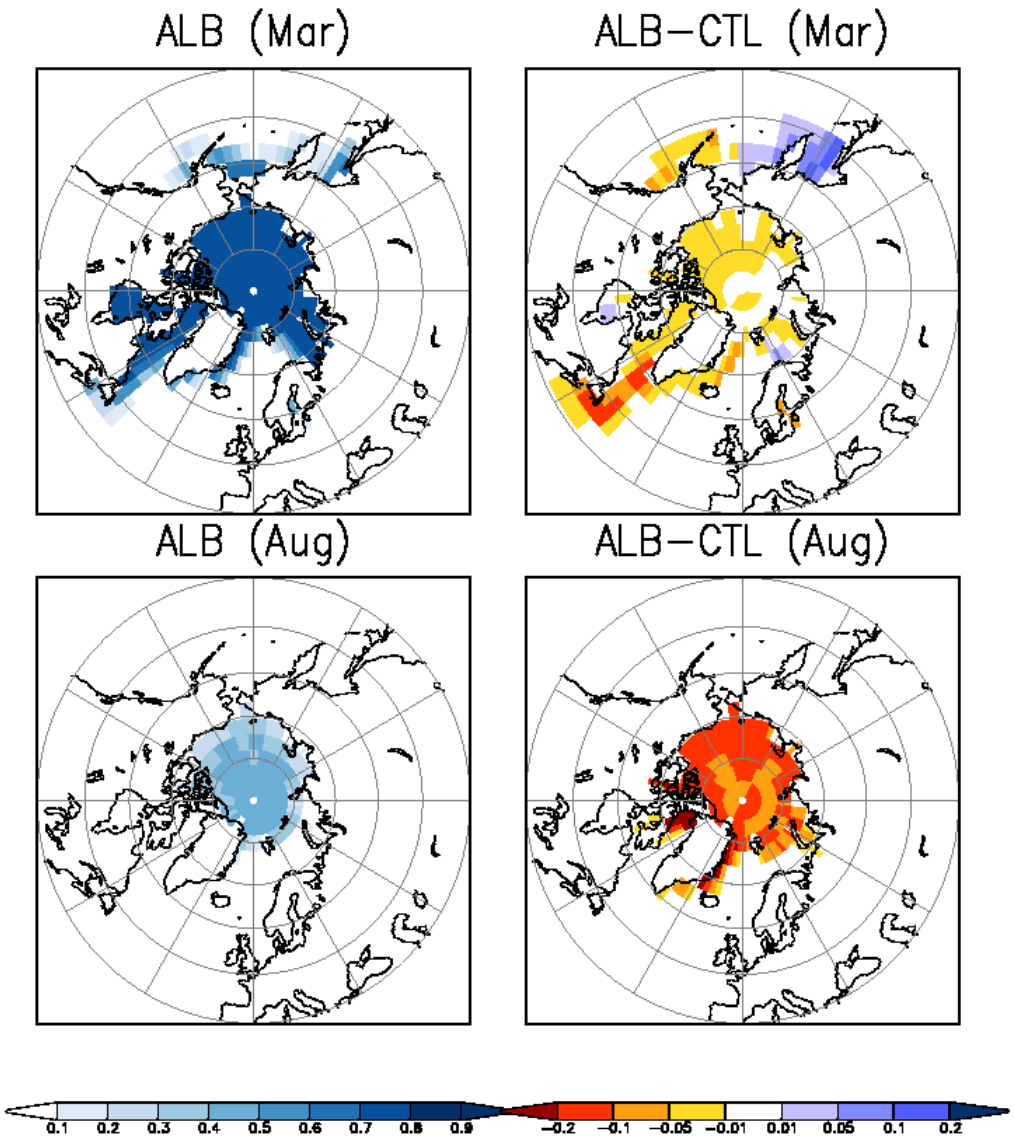

Fig. 7. Sea-ice albedo (excluding open water) in the northern hemisphere for the new albedo scheme (ALB, left) and the difference between the new and old albedo scheme (ALB-CTL, right), for March (upper panels) and July (lower panels).

datasets [McLaren et al., 2006]) with thicknesses up to 4.0 m. Thin ice in March is found south of 70°N in the Bering Sea and western part of North Atlantic Ocean. In September the thin FYI has melted, and only small areas with thin ice is found in the Barents Sea, northern Baffin Labrador and along the eastern coast of Greenland. The ALB scheme overall reduces the ice thickness, except for the Barents and Okhotsk, where the ice thickness is slightly increased in March. The absolute reductions are largest for the thick ice in the Central Arctic and smallest on the ice edge in March. In September the ice thickness is reduced everywhere, with largest reductions for the thin ice areas in Beaufort and East Greenland. The absolute changes are smallest in

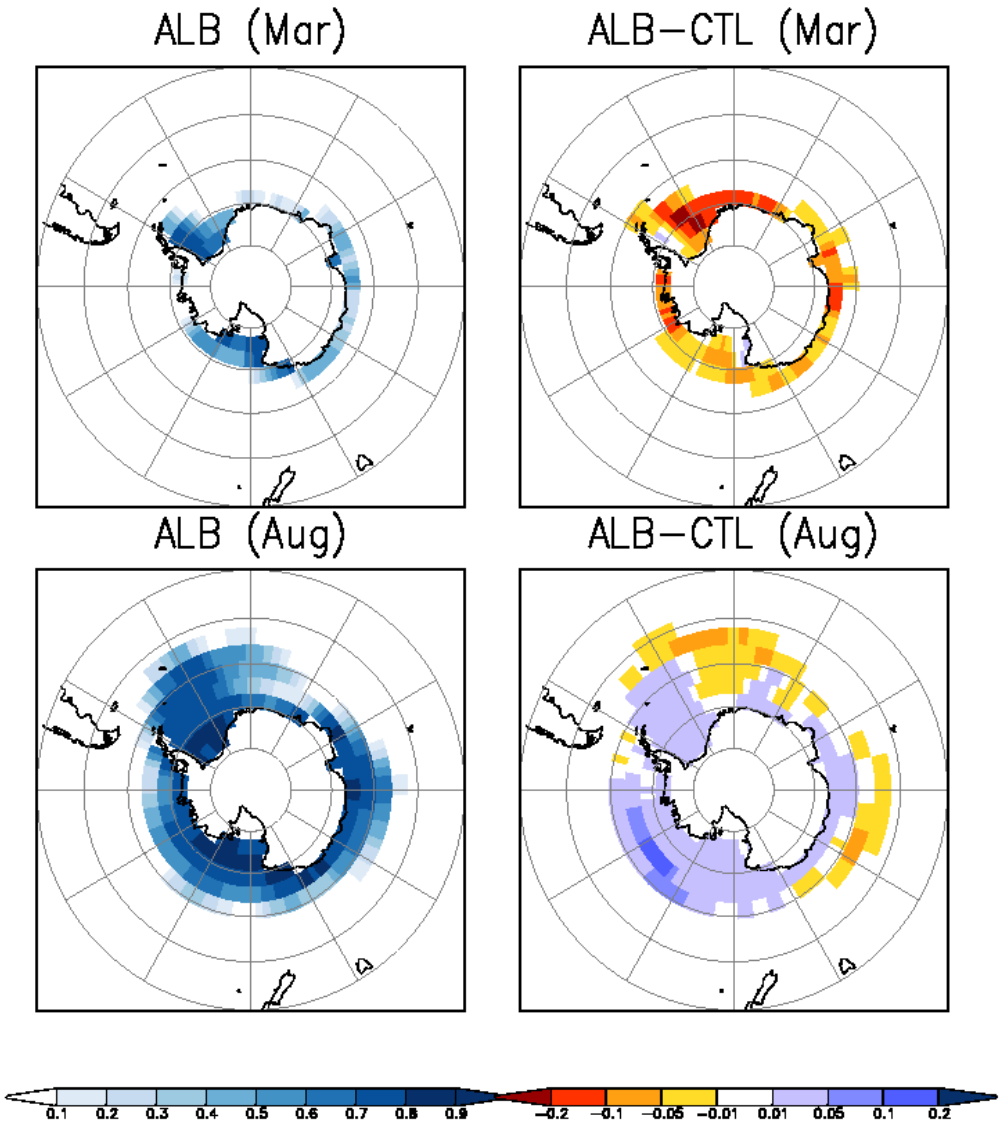

Fig. 8. Sea-ice albedo (excluding open water) in the southern hemisphere for the new albedo scheme (ALB, left) and the difference between the new and old albedo scheme (ALB-CTL, right), for March (upper panels) and July (lower panels).

the thin ice areas in Barents.

The ice in the SH is overall thinner, however thick multi-year ice is found along the coasts, particularly in the Weddell Sea at the west coast and in Amery Bay at the east coast during the whole year. Most of the sea ice in the SH is thin FYI between 0.5-1 meter thick. The ALB scheme reduce the thickness along the coast, particularly in the Antarctic summer in March. However, in the western parts of the Weddell Sea the ALB scheme increase the thickness by as much as 0.2-0.4 in March.

The probability density functions (PDFs) show in a clear way the difference

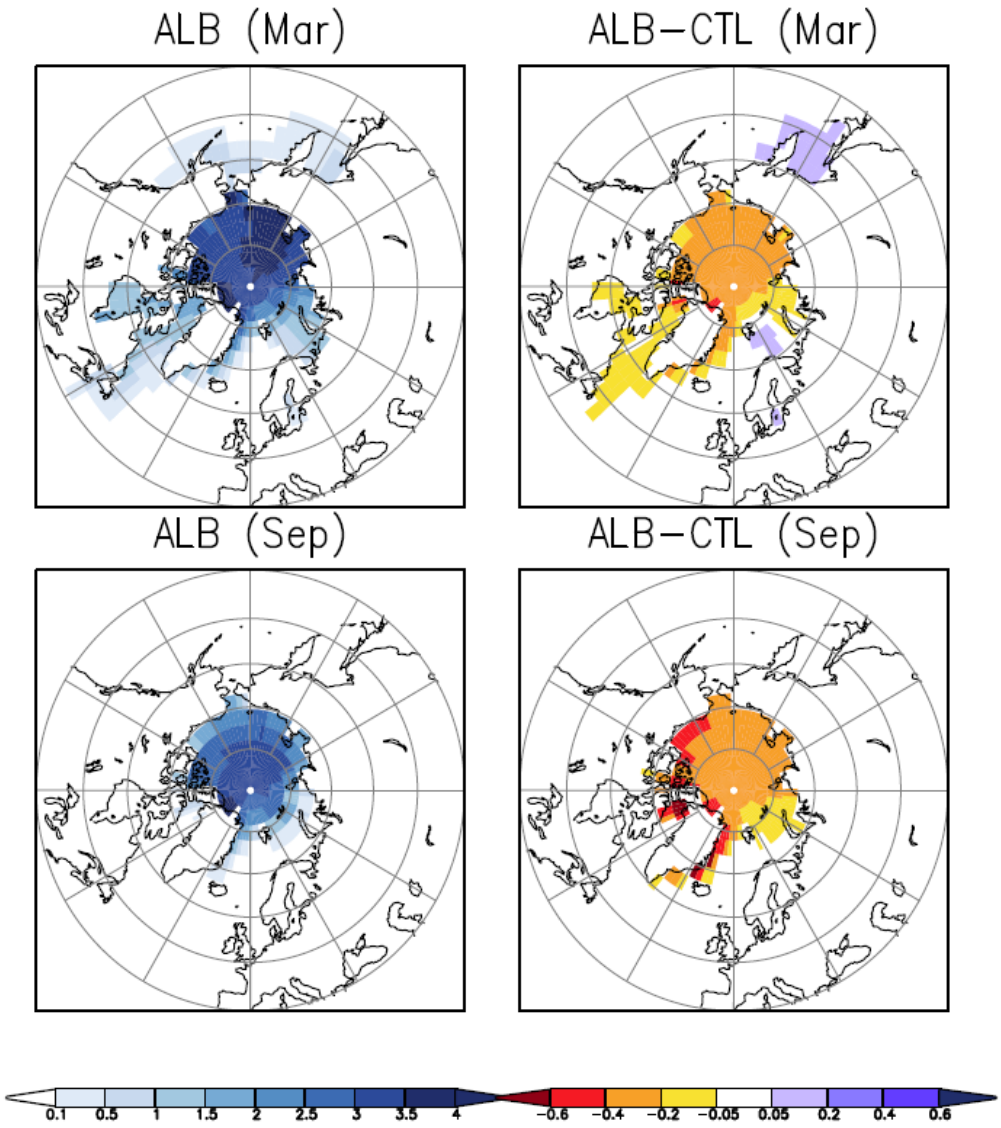

Fig. 9. Sea-ice thickness (m) in the northern hemisphere for the new albedo scheme (ALB, left) and the difference between the new and old albedo scheme (ALB-CTL, right), for March (upper panels) and September (lower panels).

between the ice thickness distributions for ALB and CTL (Figure 11). The PDFs for NH has a bimodal distribution, with the first peak at 0.13 m for ALB and CTL, and the second peaks at 3.38 m and 3.63 m for ALB and CTL in March, respectively. In September the second peaks are slightly shifted towards thinner ice. For NH, the ALB scheme leads to more thin ice and less thick ice. The ice thickness distribution for the SH is unimodal, with a peak for thin ice and very little thick ice (due to most of the sea-ice in the SH being FYI). The frequency of the thin ice is slightly reduced with the ALB scheme (opposite of what we see in NH), and a slight increase in intermediate ice thicknesses can be seen.

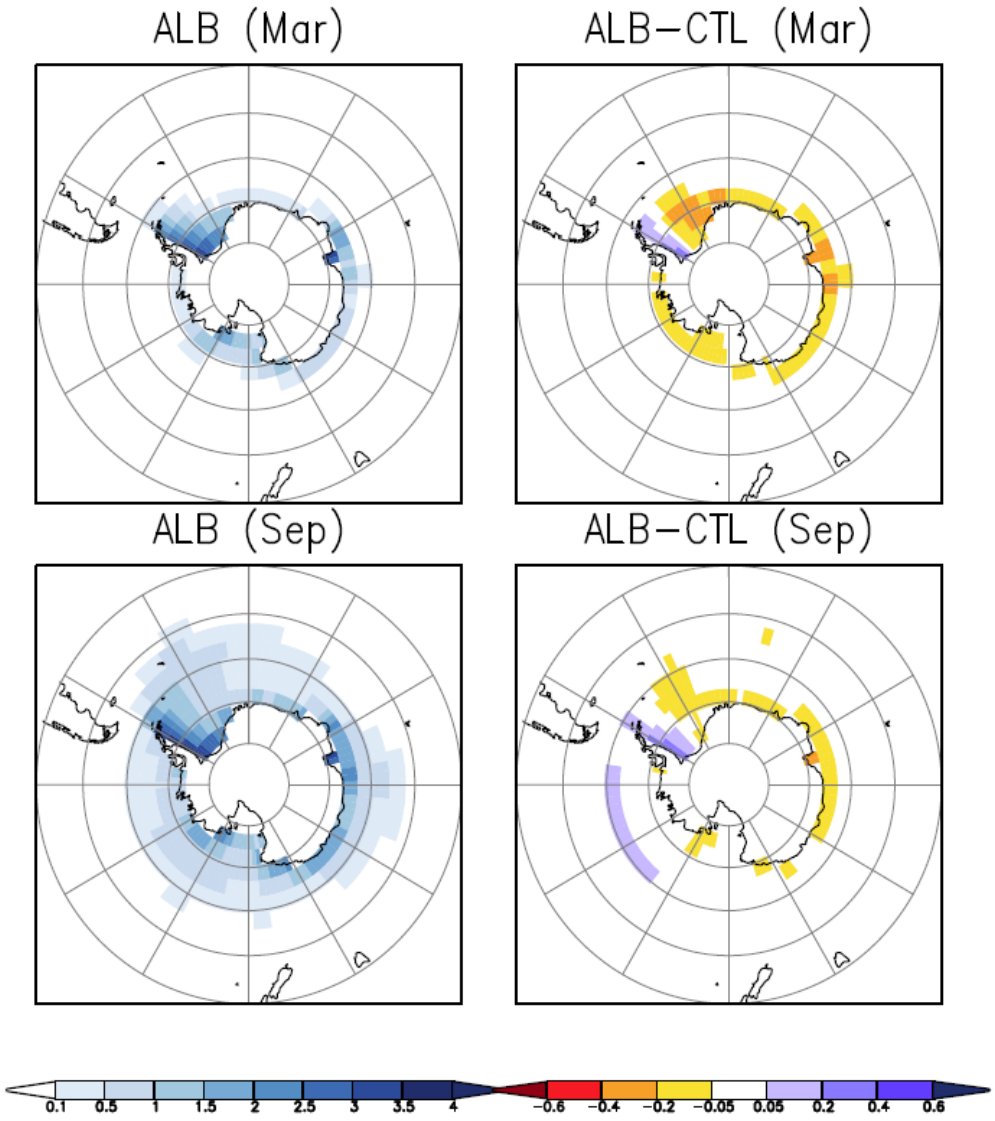

Fig. 10. Sea-ice thickness (m) in the southern hemisphere for the new albedo scheme (ALB, left) and the difference between the new and old albedo scheme (ALB-CTL, right), for March (upper panels) and September (lower panels).

3.2.4 Sea-ice concentration

The sea-ice area has a strong seasonal cycle (Figure 5d), with sea ice covering almost the whole Arctic Basin in March. In September all the FYI is melted and the ice is mainly concentrated north of 70°N, and even further north in areas affected by the North Atlantic Current (Figure 12). In March the ALB scheme reduce the sea-ice concentration south and east of Greenland, but increases it in Barents, Bearing and Okhotsk. The overall effect is thus increasing concentrations in winter. In June there is a shift, and the overall effect is reduced concentrations (Figure 5d). In September, the concentration

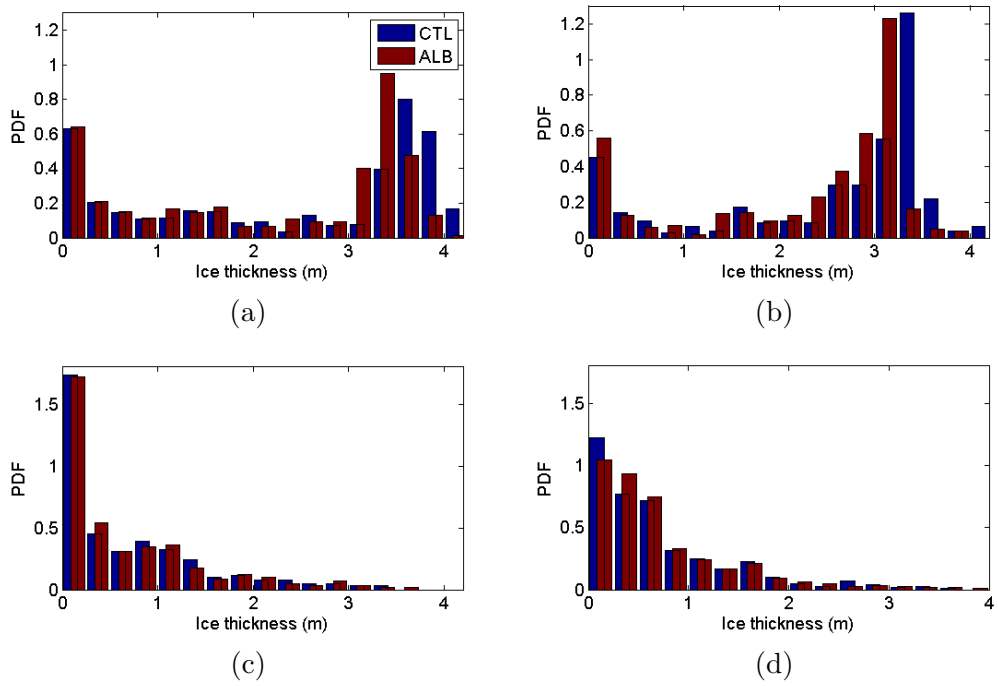

Fig. 11. Probability density functions (PDFs) for sea-ice thickness in CTRL and ALB for northern hemisphere in March (a) and September (b), and for southern hemisphere in March (c) and September (d).

is reduced along the coast areas towards the Arctic Basin, but not in the central Arctic itself, and by as much as -0.2 in northern Baffin Labrador and the east coast of Greenland. The areas of changes have strong interannual variability, and relatively low ice concentrations.

Despite the sea ice in SH being thin it is compact and the ice concentration is relative high (0.8-0.9), except on the ice edge. The ALB scheme reduce the concentration along the coast in Antarctic summer (March), except (one pixel) in the Weddell Sea. In September, the overall changes are small (Figure 5d), with decreased ice concentration north of the continent, and increased concentrations west- south-west of the continent. Compared to sea-ice concentrations from HadGEM1 [McLaren et al., 2006], both the ALB and CTL schemes give substantial less ice in the SH.

3.2.5 Statistical significance

An adapted statistical scale-space technique [Pedersen et al., 2007a] has been applied on the difference field between sea-ice parameters from the ALB and CTL schemes, to investigate if the changes introduced by the new sea-ice albedo scheme is in fact of statistical significance. The scale-space technique only requires the difference field and the interannual variability of the difference field as input, and provides maps of areas of statistical significance at

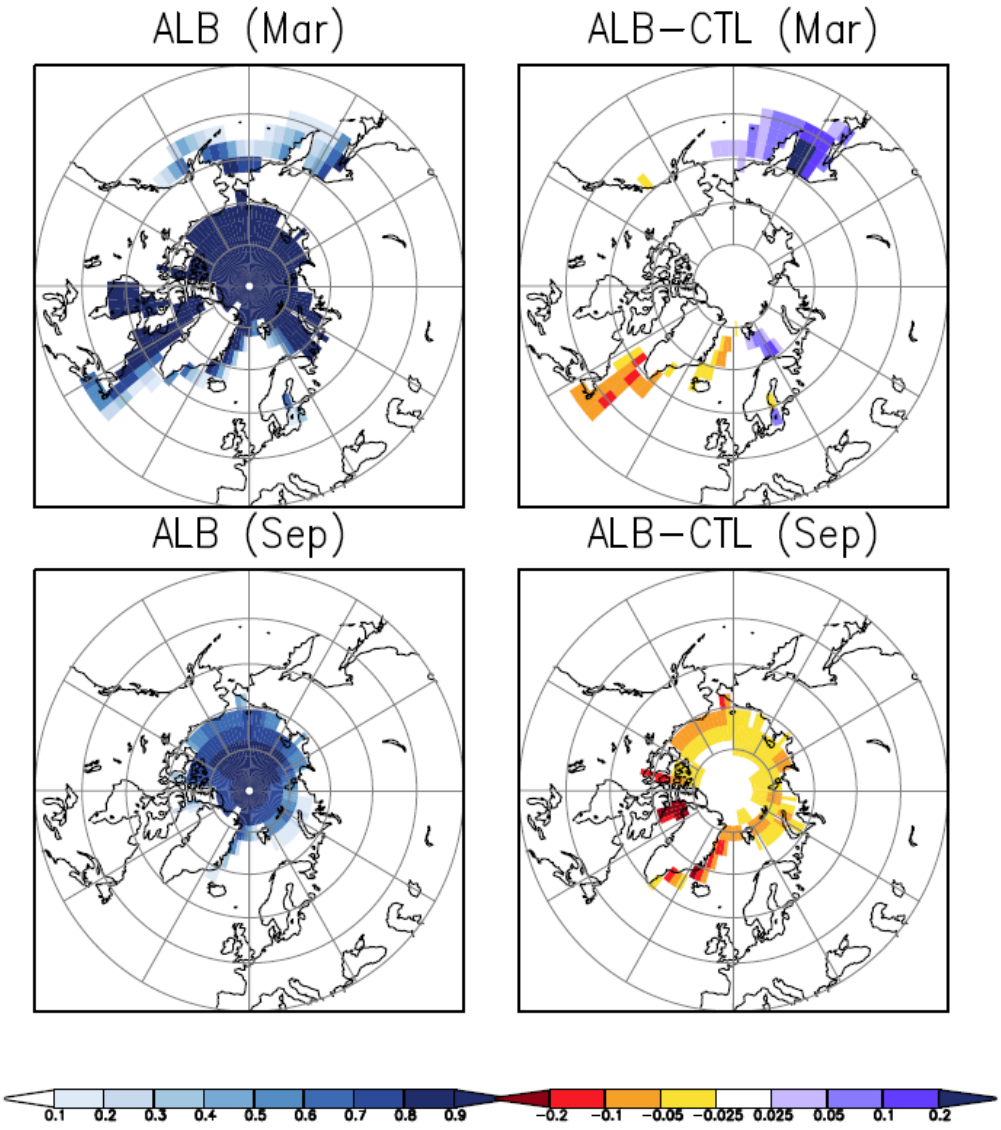

Fig. 12. Sea-ice concentration (%) in the northern hemisphere for the new albedo scheme (ALB, left) and the difference between the new and old albedo scheme (ALB-CTL, right), for March (upper panels) and September (lower panels).

different spatial scales for a given confidence level (here the common 5% is used). The scaling issue is introduced since at finer scales there is usually a large amount of noise, whereas successively coarser scales smooth the data and reduce the noise. However at very coarse scales interesting features can be smoothed away entirely. The four investigated scales are 280 km, 1100 km, 2500 km and 4000 km.

The new sea-ice albedo (ALB) is statistically significantly lower than the old (CTL), particularly in NH during summer melting, but also for some areas in spring and autumn. Statistical significant changes occur in northern Baffin

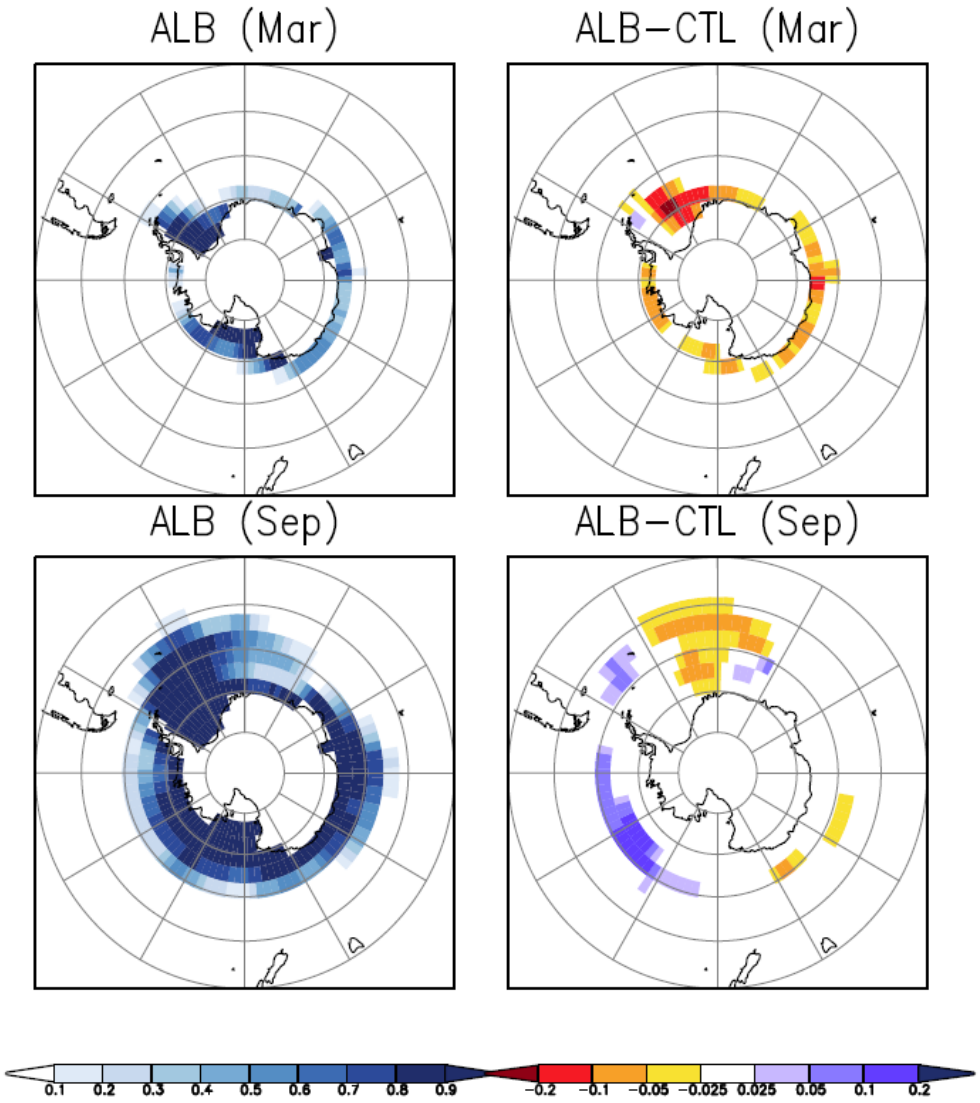

Fig. 13. Sea-ice concentration (%) in the southern hemisphere for the new albedo scheme (ALB, left) and the difference between the new and old albedo scheme (ALB-CTL, right), for March (upper panels) and September (lower panels).

Labrador for the whole year for the two largest scales. As the winter season turns into spring and summer, the areas of significant changes grow, and includes Central Arctic with the adjacent seas, except East Greenland in May. In June, only areas in Baffin Labrador are significant, but as melt ponds evolve, the areas expand to include southern East Greenland and sea areas north of Alaska in July, and pretty much all sea-ice covered areas in September, with significance for the three largest scales down to 1100 km for southern Beaufort and E. Siberia and Chukchi. When the melt ponds dry up and snow again cover the NH, only areas in northern Baffin Labrador are significant for the two largest scales. Some areas of difference are found for SH summer (January-March) in the Weddell Sea, where ALB albedo is significantly lower

than CTL albedo. In winter a few pixels are found where the ALB albedo are significantly higher than the CTL albedo (*i.e.* opposite of the general trend) in the Weddell Sea and Ross Sea for the largest scale.

The changes in sea-ice thickness are significant over large areas in the Central Arctic, Beaufort, E. Siberian Chukchi and Baffin Labrador for the coarsest scale over the entire year. In autumn and early winter the areas of significant changes expand further south in Bering. The changes occurring in the Central Arctic and northern Baffin Labrador is significant at a finer scale of 2500 km. From March to May the area extent of significant changes is at its minimum, while it has its largest extent during surface melting in July-September. Only some small areas in western Baffin Labrador is significant for the scale of 1100 km in melting peak season July and August. At the scale equal to the grid resolution, no changes are found to be significant. Fewer areas of significant changes are detected when concerning sea-ice concentration. Only for June to October significant changes appear in Baffin Labrador for the coarsest scale. In mid-summer the areas of significant changes expand further west to include eastern Hudson Bay (which is also significant for finer scales in July-September).

No areas of significantly differences were found for ice thickness nor ice area in the SH. This confirms the previous results that melt ponds are dominant in the NH, and play a minor role in the SH.

4 Summary and discussion

It has previously been recognized that GCMs are unable to predict the annual cycle of sea-ice albedo completely, and that the albedo particularly is too large in summer [Køltzow, 2007, Curry et al., 2001]. Wang et al. [2006] found that the IPCC 4AR climate models systematically overestimate the sea-ice albedo in summer with as much as 0.05, and in winter, large discrepancies exist between the models. To the authors knowledge no GCM includes an explicit treatment of melt ponds on the sea ice in summer. Despite the relative short duration of melt ponds, they contributes largely to the energy balance because the albedo effect on the climate is largest in summer due to the high irradiance. For the northernmost and southernmost latitudes in the respective winters the Sun is below the horizon and the albedo effect is very small.

We have developed a physically based sea-ice albedo parameterization scheme for ECHAM5 GCM following the structure of the sea-ice albedo in a thermodynamic sea-ice model [Schramm et al., 1997], which separated between snow covered sea ice, bare sea ice, melt ponds and open water. The new albedo scheme (ALB) is found to reduce the sea-ice albedo both in winter due to

snow ageing and in summer due to melt ponds, compared to the old albedo scheme (CTL). Also the spring decay and autumn increase of sea-ice albedo is captured in a more realistic way in the new scheme. The new albedo parameterization simulated the annual cycle of sea-ice albedo in a realistic way, capturing the important transition changes to determine the onset of melt, the duration of melt and the start of the fall freeze-up [Perovich et al., 2002a]. The correlation coefficient between the one year sea-ice albedo simulations (ALB) and one year observations at the SHEBA site [Perovich et al., 2002a] was 0.83, where the ALB albedo was slightly higher than the observed albedo in summer. The SHEBA albedo may represent a lower boundary for albedo during summer. When compared to the albedo from several decades of Soviet NP drifting ice stations data, SHEBA albedo was slightly lower than the monthly minimum albedo for mid-June to mid-September [Perovich et al., 2002a]. However, the minimum albedo was slightly shifted in time in the NP dataset, and where the ECHAM5 and SHEBA albedo have their minimum in August - mid-August the minimum albedo for the NP stations was in mid-July. Note however that there are large interannual variability in the ECHAM5 model. This implies there are years when hardly any melt pond forms, while in others the formation starts already in early June and reaches depth up to 0.5 m in August, so we should be careful about conclusions based on a single year.

The overall effect on the sea-ice albedo was largest in summer, with average reductions of 23%, or 0.14, in NH in August. In SH the overall effect was less. However, the albedo was reduced in Antarctic winter due to snow ageing. In summer some melt ponds were present, however, they had a much shorter duration and covered less areas compared to the NH. Still, relative large albedo reductions were found in the Weddell Sea, and overall the sea-ice albedo in SH in February was reduced by 12%.

The new albedo scheme performed well in modeling the coverage of melt ponds compared to the observation at the SHEBA site both when looking at the temporal evolution and the mean area covered. For the entire NH the coverage was on the low side compared to observations, but gave for the first time an estimate of the spatial variability of the melt pond coverage. The inclusion of melt ponds and reductions in albedo were dominant on the FYI areas, as melt ponds tend to cover larger areas on FYI, and also because the overall effect of replacing thin ice with open water gives a huge impact on the energy balance. However, the melt ponds tend to be shallower on FYI, which may result in less reduction of the albedo. Also, per definition, the FYI will melt away during the summer, therefore the relative effect of MYI could be greater. This remains to be investigated. If the melt ponds increase the length of the melt season, they may largely contribute to the albedo feedback process, as regression equations implies that one extra day of melting results in an extra 4.9 cm of summer ice melt. [Laxon et al., 2003].

The effect of reduced sea-ice albedo is overall reduced sea-ice thickness, concentration and volume, with large temporal and spatial variations. *E.g.* in the Barents and Okhotsk the sea-ice albedo increases in March, giving an increasing sea-ice thickness and concentration for these areas (Figures 7, 9, 12). In September the pattern is more spatially homogeneously with reduced albedo, thickness and concentrations for all areas where the new ALB scheme gives an effect. The reductions in ice thickness are up to 0.4-0.5 m for Central Arctic for December-June, with largest reductions (up to 1.0 m) in the East Greenland, Baffin Labrador and Beaufort in late autumn. The thin ice with relative low concentration along the southern east coast of Greenland disappears completely in September due to the new ALB scheme. It is, however, difficult to assess the distribution and seasonal cycles of sea-ice thickness, because of few consistent ice thickness datasets. A previous study using satellite altimeter measurements of ice freeboard [Laxon et al., 2003], found the average winter ice thickness (excluding thin ice below 1 meter) over sea-ice areas for NH south of 81.5°N for the 8-years 1993-2001 to be 2.7 m. The thickest ice was observed in the Canadian Archipelago and in the Fram Strait. There are however two problems with assessing the simulations of sea-ice parameters in the model and forcing used here against observational datasets. First, the observations are for present day climate, whereas the model simulations uses pre-industrial climate forcings. *E.g.* simulations suggest that mean ice thickness has declined 0.4 m since 1860 [McLaren et al., 2006]. Second, the time period for the observations are relative short, thus it may not reflect the long term state as the 50 years average we investigate. However, we would like to increase the number of simulated years to remove sampling artifacts.

The effect from the new ALB scheme on a few global climate variables can be seen in Table 5. Overall the relative differences are largest for sea-ice surface melting in the NH (+6.4%) and SH (-12.2%). The sea-ice thickness is reduced with 8.7% in NH and 3.0% in SH, while the sea-ice areas are reduced by 1.7% in NH and 2.3% in SH. The global surface albedo is reduced with 1%, while for the other parameters only very small changes occur.

Some further topics remain to be investigated, particularly concerning the melt ponds. We would like to investigate the melt pond coverage and evolution separately for FYI and MYI, and also to study in more details the spatial variability in the observed fractional coverage of melt ponds. We also plan to discuss more on the impacts and implications our results has for climate change results.

Variable	CTL	ALB	Units
Sea ice area (NH)	10.89	10.71	10^{12} m^2
Sea ice area (SH)	11.93	11.66	10^{12} m^2
Sea ice thickness (NH)*	2.41	2.20	m
Sea ice thickness (SH)*	0.99	0.96	m
Sea ice surface melting (NH)*	8.29	8.82	Wm^{-2}
Sea ice surface melting (SH)*	3.12	2.74	Wm^{-2}
Surface sensible heat flux	18.20	18.21	Wm^{-2}
Surface latent heat flux	79.96	79.94	Wm^{-2}
Surface net solar radiation	154.68	154.78	Wm^{-2}
Surface net longwave radiation	-55.21	-55.25	Wm^{-2}
Surface albedo	13.75	13.61	%
TOA net solar radiation	232.94	232.99	Wm^{-2}
TOA outgoing longwave	231.10	231.07	Wm^{-2}
TOA shortwave cloud forcing	-49.59	-49.93	Wm^{-2}
TOA longwave cloud forcing	28.77	28.79	Wm^{-2}
Planetary albedo	31.85	31.84	%
Surface air temperature	13.56	13.55	°C
Precipitation	2.75	2.75	mmd^{-1}

Table 5
Comparison of pre-industrial T31 runs (50-years global annual means), where CTL is control simulation and ALB is new sea-ice albedo scheme. * is averaged over sea-ice areas only.

Acknowledgement

We would like to thank Renate Brokopf for preparing the model data and some of the figures, and S. Gerland for comments on the work. A. C. Roesch, M. Køltzow, B. Ivanov and D. K. Hall are acknowledged for comments during an early stage of this work. This work was supported by the Research Council of Norway, the Norwegian Polar Institute and the University of Tromsø.

References

E. L. Andreas and S. F. Ackley. On the Differences in Ablation Seasons of Arctic and Antarctic Sea Ice. *Journal of Atmospheric Science*, 39:440–447,

1982.

D. G. Baker, D. L. Ruschy, and D. B. Wall. The Albedo Decay of Prairie Snows. *Journal of Applied Meteorology - Notes and Correspondence*, 29: 179–187, 1990.

D.G. Barber and J. Yackel. The Physical, Radiative and Microwave Scattering Characteristics of Melt Ponds on Arctic Landfast Sea Ice. *International Journal of Remote Sensing*, 20(10):2069–2090, 1999.

R. G. Barry. The Parameterization of Surface Albedo for Sea Ice and its Snow Cover. *Progress in Physical Geography*, 20(1):63–79, 1996.

R. E. Brandt, S. G. Warren, A. P. Worby, and T. C. Grenfell. Surface Albedo of the Antarctic Sea Ice Zone. *Journal of Climate*, 18:3606–3622, 2005.

J. Comiso. Abrupt Decline in the Arctic Winter Sea Ice Cover. *Geophysical Research Letter*, 33(L18504), 2006.

J. Curry, J. L. Schramm, and E. E. Ebert. Sea Ice-Albedo Climate Feedback Mechanism. *Journal of Climate*, 8:240–247, February 1995.

J. A. Curry, J. L. Schramm, D. K. Perovich, and J. O. Pinto. Applications of SHEBA/FIRE Data to Evaluation of Snow/Ice Albedo Parameterizations. *Journal of Geophysical Research*, 106(D14):15345–15355, July 2001.

C. Derksen, J. Piwowar, and E. LeDrwe. Sea-Ice Melt-Pond Fraction as Determined from Low Level Aerial Photographs. *Arctic and Alpine Research*, 29(3):345–351, 1997.

R. E. Dickinson, A. Henderson-Sellers, P. J. Kennedy, and M. F. Wilson. Biosphere Atmosphere Transfer Scheme (BATS) for the NCAR Community Climate Model. Technical report, NCAR Technical Note NCAR/TN-275+STR, 1986. 69 pp.

R. E. Dickinson, A. Henderson-Sellers, and P. J. Kennedy. Biosphere Atmosphere Transfer Scheme (BATS) Version 1e as Coupled to the NCAR Community Climate Model. Technical report, NCAR Technical Note NCAR/TN-387+STR, 1993. 72 pp.

H. Eicken, T. C. Grenfell, D. K. Perovich, J. A. Richter-Menge, and K. Frey. Hydraulic Controls of Summer Arctic Pack Ice Albedo. *Journal of Geophysical Research*, 109(C08007), August 2004.

F. Fetterer and N. Untersteiner. *IGARSS '98: Sensing and Managing the Environment*, chapter Melt Pond Coverage Statistics from Classified Satellite Data, pages 1954–1956. IEEE International Geoscience and Remote Sensing Symposium Proceedings, 1998a.

F. Fetterer and N. Untersteiner. Observations of Melt Ponds on Arctic Sea Ice. *Journal of Geophysical Research*, 103(C11):24821–24835, October 1998b.

S. Gerland, J.-G. Winther, J. B. rbk, G. E. Liston, N. A. ritsland, A. Blanco, and B. Ivanov. Physical and Optical Properties of Snow Covering Arctic Tundra on Svalbard. *Hydrological Processes*, 13:2331–2343, 1999.

S. Gerland, C. Haas, M. Nicolaus, and J.-G. Winther. Seasonal Development of Structure and Optical Properties of Fast Ice in Kongsfjorden, Svalbard. In C. Wiencke, editor, *The Coastal Ecosystems of Kongsfjorden, Svalbard*, number 492, pages 26–34. Alfred Wegner Institute for Polar & Marine Re-

search, 2004.

S. Gerland, J. Aars, T. Bracegirdle, E. Carmack, H. Hop, G. K. Hovelsrud, K. M. Kovacs, C. Lydersen, D. K. Perovich, J. Richter-Menge, S. Rybråten, H. Strøm, and J. Turner. *Global Outlook for Ice and Snow*, chapter Ice in the Sea (Chapter 5), pages 63–96. UN Environment Program (UNEP), 2007.

J. M. Hanesiak, D. G. Barber, R. A. De Abreu, and J. J. Yackel. Local and Regional Albedo Observations of Arctic First-Year Sea Ice during Melt Ponding. *Journal of Geophysical Research*, 106(C1):1005–1016, 2001a.

J. M. Hanesiak, J. J. Yackel, and D. G. Barber. Effect of Melt Ponds on First-Year Sea Ice Ablation - Integration of RADARSAT-1 and Thermodynamic Modelling. *Canadian Journal of Remote Sensing*, 27(5):433–442, October 2001b.

W.D. III Hibler. A Dynamic Thermodynamic Sea Ice Model. *Journal of Physical Oceanography*, 9:815–846, 1979.

J. H. Jungclaus, N. Keenlyside, M. Botzet, H. Haak, J.-J. Luo, M. Latif, J. Marotzke, U. Mikolajewicz, and E. Roeckner. Ocean Circulation and Tropical Variability in the Coupled Model ECHAM5/MPI-OM. *Journal of Climate*, 19:3952–3972, 2006.

M. Køltzow. The Effect of a New Snow and Sea Ice Albedo Scheme on Regional Climate Model Simulations. *Journal of Geophysical Research*, 112(D07110), April 2007.

S. Laxon, N. Peacock, and D. Smith. High Interannual Variability of Sea Ice Thickness in the Arctic Region. *Nature*, 425(30):947–950, October 2003.

M. Lüthje, D. L. Feltham, P. D. Taylor, and M. G. Worster. Modeling the Summertime Evolution of Sea-Ice Melt Ponds. *Journal of Geophysical Research*, 111(C02001), 2006.

T. Markus, D. J. Cavalieri, and A. Ivanoff. The Potential of Using Landsat 7 ETM+ for the Classification of Sea-Ice Surface Conditions during Summer. *Annals of Glaciology*, 34:415–419, 2002.

T. Markus, D. J. Cavalieri, M. A. Tschudi, and A. Ivanoff. Comparison of Aerial Video and Landsat 7 Data over Ponded Sea Ice. *Remote Sensing of Environment*, 86(4):458–469, August 2003.

S. J. Marsland, H. Haak, J. H. Jungclaus, M. Latif, and F. Röske. The Max-Planck-Institute Global Ocean/Sea Ice Model with Orthogonal Curvilinear Coordinates. *Ocean Modelling*, 5:91–127, 2003.

A. J. McLaren, H. T. Banks, C. F. Durman, J. M. Gregory, T. C. Johns, A. B. Keen, J. K. Ridley, M. J. Roberts, W. H. Lipscomb, W. M. Connolley, and S. W. Laxon. Evaluation of the Sea-Ice Simulations in a New Coupled Atmosphere-Ocean Climate Model (HadGEM1). *Journal of Geophysical Research*, 111(C12014), 2006.

M. P. Morassutti and E. F. Le Drew. Albedo and Depth of Melt Ponds on Sea Ice. *International Journal of Climatology*, 16:817–838, 1996.

J. Overland and M. Wang. Future Regional Arctic Sea Ice Declines. *Geophysical Research Letters*, 34(L17705), 2007.

C. A. Pedersen and J.-G. Winther. Intercomparison and Validation of Snow Albedo Parameterisation Schemes in Climate Models. *Climate Dynamics*, 25:351–362, 2005.

C. A. Pedersen, F. Godtliebsen, and A. C. Roesch. A Scale-Space Approach for Detecting Significant Differences between Models and Observations Using Global Albedo Distributions. Accepted, Journal of Geophysical Research, 2007a.

C. A. Pedersen, R. Hall, S. Gerland, A. H. Sivertsen, T. Svenøe, and C. Haas. Combined Airborne Profiling over Fram Strait Sea Ice: Fractional Sea-Ice Types, Albedo and Thickness Measurements. Submitted, Cold Regions Science and Technology, Oct., 2007b.

D. K. Perovich and W. B. III Tucker. Arctic Sea-Ice Conditions and the Distribution of Solar Radiation during Summer. *Annals of Glaciology*, 25: 445–450, 1997.

D. K. Perovich, E. I. Andreas, J. A. Curry, H. Eicken, C. W. Fairall, T. C. Grenfell, P. S. Guest, J. Intrieri, D. Kadko, R. W. Lindsay, M. G. McPhee, J. Morison, R. E. Moritz, C. A. Paulson, W. S. Pegau, P. O. G. Persson, R. Pinkel, J. A. Richter-Menge, T. Stanton, H. Stern, M. Sturm, W. B. III Tucker, and T. Uttal. Year on Ice Gives Climate Insights. *EOS, Transactions, American Geophysical Union*, 80(41), October 1999.

D. K. Perovich, T. C. Grenfell, B. Light, and P. V. Hobbs. Seasonal Evolution of the Albedo of Multiyear Arctic Sea Ice. *Journal of Geophysical Research*, 107(C10), 2002a.

D. K. Perovich, W. B. III Tucker, and K. A. Ligett. Aerial Observations of the Evolution of Ice Surface Conditions during Summer. *Journal of Geophysical Research*, 107(C10):8048–8062, October 2002b.

N. A. Rayner, D. E. Parker, E. B. Horton, C. K. Folland, L. V. Alexander, D. P. Rowell, E. C. Kent, and A. Kaplan. Global Analyses of Sea Surface Temperature, Sea Ice and Night Marine Air Temperature since the Late Nineteenth Century. *Journal of Geophysical Research*, 108(D14):4407, 2003.

E. Roeckner, G. Bäuml, L. Bonaventura, R. Brokopf, M. Esch, M. Giorgetta, S. Hagemann, I. Kirchner, L. Kornblueh, E. Manzini, A. Rhodin, U. Schlese, U. Schulzweida, and A. Tompkins. The Atmospheric General Circulation Model ECHAM5 - Part 1. Technical Report 349, Max Planck Institute for Meteorology, 2003.

E. Roeckner, R. Brokopf, M. Esch, M. Giorgetta, S. Hagemann, L. Kornblueh, E. Manzini, U. Schlese, and U. Schulzweida. Sensitivity of Simulated Climate to Horizontal and Vertical Resolution in the ECHAM5 Atmosphere Model. *Journal of Climate*, 19:3771–3791, 2006.

A. Roesch, M. Wild, H. Gilgen, and A. Ohmura. A New Snow Cover Fraction Parameterisation for the ECHAM4 GCM. *Climate Dynamics*, 17:933–946, 2001.

A. C. Roesch. *Assessment of the Land Surface Scheme in Climate Models with Focus on Surface Albedo and Snow Cover*. PhD thesis, Swiss Federal Institute of Technology Zurich, 2000.

J. L. Schramm, M. M. Holland, J. A. Curry, and E. E. Ebert. Modeling the Thermodynamics of a Sea-Ice Thickness Distribution - 1. Sensitivity to Ice Thickness Resolution. *Journal of Geophysical Research*, 102(C10):23079–23091, October 1997.

SHEBA melt pond, 2007. Surface Heat Energy Balance of the Arctic Ocean - Melt Pond. http://www.crrel.usace.army.mil/sid/perovich/SHEBAice/meltpond.htm), 2007. Accesses December, 2007.

SMIP, 2006. Snow Modelers Internet Platform. http://www.geo.utexas.edu/climate/Research/SNOWMIP/, 2006. Accessed December, 2006.

S. Solomon, D. Qin, M. Manning, R. B. Alley, T. Berntsen, N. L. Bindoff, Z. Chen, A. Chidthaisong, J. M. Gregory, G. C. Hegerl, M. Heimann, B. Hewitson, B. J. Hoskins, F. Joos, J. Jouzel, V. Kattsov, U. Lohmann, T. Matsuno, M. Molina, N. Nicholls, J. Overpeck, G. Raga, V. Ramaswamy, J. Ren, M. Rusticucci, R. Somerville, T. F. Stocker, P. Whetton, R. A. Wood, and D. Wratt. Technical summary. in: Climate change 2007: The physical science basis. contribution of working group i to the fourth assessment report of the intergovernmental panel on climate change. Technical report, Cambridge University Press, Cambridge, United Kingdom and New York, NY, USA, 2007.

J. Stroeve, M. M. Holland, W. Meier, T. Scambos, and M. Serreze. Arctic Sea Ice Decline: Faster than Forecast. *Geophysical Research Letter*, 34(L09501), 2007.

P. D. Taylor and D. L. Feltham. A model of Melt Pond Evolution on Sea Ice. *Journal of Geophysical Research*, 109(C12007), December 2004.

M. A. Tschudi, J. A. Curry, and J. A. Maslanik. Airborne Observations of Summertime Surface Features and Their Effect on Surface Albedo during FIRE/SHEBA. *Journal of Geophysical Research*, 106(D14):15335–15344, July 2001.

M.A. Tschudi, J. A. Curry, and J. A. Maslanik. Determination of Areal Surface-Feature Coverage in the Beaufort Sea using Aircraft Video Data. *Annals of Glaciology*, 25:434–438, 1997.

W. B. III Tucker, A. J. Gow, D. A. Meese, and H. W. Bosworth. Physical Characteristics of Summer Sea Ice Across the Arctic Ocean. *Journal of Geophysical Research*, 104:1489–1504, 1999.

S. Wang, A. T. Trishchenko, K. V. Khlopenkov, and A. Davidson. Comparison of International Panel on Climate Change Fourth Assessment Report Climate Model Simulations of Surface Albedo with Satellite Products over Northern Latitudes. *Journal of Geophysical Research*, 111(D21108), 2006.

S. G. Warren. Optical Properties of Snow. *Reviews of Geophysics and Space Physics*, 20(1):67–89, 1982.

W. J. Wiscombe and S. G. Warren. A Model for the Spectral Albedo of Snow. I: Pure Snow. *Journal of the Atmospheric Science*, 37:2712–2733, 1980.

J. O. Wolff, E. Maier-Reimer, and S. Legutke. The Hamburg Ocean Primitive

Equation Model HOPE. Technical Report 13, German Climate Computer Center (DKRZ), Hamburg, Germany, 1997.

J. J. Yackel and D. G. Barber. Melt Ponds on Sea-Ice in the Canadian Archipelago 2. On the Use of RADARSAT-1 Synthetic Aperture Radar for Geophysical Inversion. *Journal of Geophysical Research*, 105(C9):22061–22070, September 2000.

J. J. Yackel, D. G. Barber, and J. M. Hanesiak. Melt Ponds on Sea-Ice in the Canadian Archipelago 1. Variability in Morphological and Radiative Properties. *Journal of Geophysical Research*, 105(C9):22049–22060, September 2000.

Z.-L. Yang, R. E. Dickinson, A. Robock, and K. Y. Vinnikov. Validation of the Snow Submodel of the Biosphere-Atmosphere Transfer Scheme with Russian Snow Cover and Meteorological Observational Data. *Journal of Climate*, 10:353–373, 1997.